Experimental measurement of dislocation density in metallic materials: A quantitative comparison between measurements techniques (XRD, R-ECCI, HR-EBSD, TEM)

J. Gallet, M. Perez, R. Guillou, C. Ernould, Christophe Le Bourlot, C. Langlois, B. Beausir, E. Bouzy, Thibaut Chaise, S. Cazottes

Experimental measurement of dislocation density in metallic materials: a quantitative comparison between measurements techniques (XRD, R-ECCI, HR-EBSD, TEM)

J. Gallet[1], M. Perez[1], R. Guillou[2], C. Ernould[3,4], C. Le Bourlot[1], C. Langlois[1], B. Beausir[3,4], E. Bouzy[3,4], T. Chaise[5] and S. Cazottes[1]

[1] Université de Lyon, INSA Lyon, UCBL, MATEIS, UMR CNRS 5510, France

[2]Université Paris-Saclay, CEA, Service de Recherches Métallurgiques Appliquées, 91191, Gif sur Yvette, France.

[3] Université de Lorraine, CNRS, LEM3, F-57000 Metz, France.

[4] Laboratory of Excellence on Design of Alloy Metals for low-mAss Structures (DAMAS), University of Lorraine, 57073 Metz, France.

[5] Univ Lyon, INSA Lyon, CNRS, LaMCoS, UMR 5259, 69621 Villeurbanne, France

Highlights:

- dislocation density measurements acquired by TEM, XRD, R ECCI, EBSD, HR EBSD
- quantitative comparison between those 5 different techniques
- capability and limits of each technique are discussed.

Abstract:

Dislocation densities were measured on the very same samples using Transmission Electron Microscopy (TEM), Scanning Electron Microscopy (Electron Channeling Contrast Imaging (ECCI) and High angular Resolution-Electron Back Scattered Diffraction (HR-EBSD)) and X-Ray Diffraction. Those different methods do not observe the same type of dislocations, i.e. Statistically Stored Dislocations (SSD) and/or Geometrically Necessary Dislocations (GND). Some are direct measurements techniques such as ECCI and TEM imaging while other are undirect methods, namely HR-EBSD and XRD measurements. Therefore, a quantitative comparison of the measurements obtained using those four techniques on undeformed and deformed duplex steels is proposed. For low deformation, where the dislocation density is quite small ($1 - 5 \times 10^{13}\ \mathrm{m}^{-2}$), imaging methods are rather performant, while XRD measurements suffer from high uncertainty levels. HR-EBSD measurements show results that are in good agreement with the other methods for those deformation levels. For higher deformation levels (with dislocation densities above $1 - 3 \times 10^{14}\ \mathrm{m}^{-2}$), imaging methods are not relevant anymore, due to the increasing uncertainty arising from local contrast variation and overlapping of dislocations. The different results obtained highlight the necessity to take a step back on each method used. Correctly defining what is to be measured (SSD or GND), in which condition (solid material or thin plate), the parameters (pixel size, area ...) and their bias is essential, especially if the objective is to use the measurement in a micromechanical model.

Keywords:

Dislocation density, ECCI, TEM, XRD, HR EBSD, EBSD

1. Introduction

The plastic deformation of materials comes from the ability of crystal lattices to shear through the movements of dislocations. The interactions of the different mechanisms of deformation, are complex and depend on each other. Their understanding is necessary and a precise observation of these phenomena must be carried out in order to take them into account when building theoretical models at the microstructural scale [1–4]. For example, Mecking *et al.* [5, 6] and Estrin *et al.* [7, 8] proposed yield strength and hardening models using the dislocation density ρ as a key parameter. Blaizot *et al.* [1, 9] confirmed experimentally that Mecking's theory could be applied to describe the impact of the dislocation density on the yield strength in the case of nickel-based alloys, while Diano *et al.* [10] experimentally showed that the tensile properties are mainly controlled by the grain size and the dislocation density.

Although different methods have been developed, experimental measurement of dislocation density in metallic alloys remains a challenging task. Indeed, for each measurement method, experimental artefacts induce non-negligible bias that must be considered. Beyond the definition of dislocations from the crystallographic point of view, their modelling implies concepts or units which differs from metallurgical ones at some point (e.g., expressing densities in m^{-1} rather than m^{-2}).

Dislocation in polycrystalline materials can usually be found either isolated, randomly distributed inside the cells or grains, or localized close to grain boundaries to accommodate possible strain incompatibilities between the different grains. Other dislocations are found to be organized into patterns, in the form of dislocation cells or walls.

Therefore the total dislocation density ρ_{tot} is often decomposed as [11, 12]:

$$\rho_{\mathrm{tot}} = \rho_W + \rho_c + \rho_{\mathrm{GB}} \quad (1)$$

with ρ_W the density of dislocations constituting the cell walls, ρ_c the dislocation density randomly distributed within the cells/grains and ρ_{GB} the dislocation density present at grain boundaries.

Another description of dislocation is often given, namely Geometrically Necessary Dislocations (GND) and Statistically Stored Dislocations (SSD), as presented by Nye [13], Cottrell [14] and Ashby [15]. GND play an important role in the strengthening effects of alloys [16, 17]. They are related to the deformation gradients due to the geometric constraints of the crystal lattice. These "same-sign" dislocations induce lattice curvature, or local disorientation, and represent dislocations more often located at grain boundaries or at cells walls so that the total amount of GND can also be expressed as $\rho_{GND} = \rho_W + \rho_{GB}$. On the other end, SSDs are stored due to an accumulation process - they trap each other randomly and do not produce significant disorientation [18]. Those dislocations represent the random distribution of dislocations, described by ρ_c. Hence, the total dislocation density is often rewritten simply as:

$\rho_{tot} = \rho_{GND} + \rho_{SSD}$.

The experimental determination of the dislocation density can be done using different methods, for instance imaging methods such as Transmission Electron Microscopy (TEM), Electron Channeling Contrast Imaging in the Scanning Electron Microscope (ECCI), or diffraction-based methods such as Electron Back Scattered Diffraction (EBSD), High Resolution-EBSD (HR-EBSD) or X-Ray Diffraction (XRD).

It should be noted, however, that each method does not characterize the same dislocation populations.

Dislocation imaging methods such as TEM or ECCI theoretically allow the observation of all the dislocations in the analyzed volume. The dislocation density is most usually performed by counting the visible dislocations on the analyzed areas, and applying a derivate of the general formula $\rho_{tot} = L/V$ [19], with *V* the analyzed volume and *L* the total dislocation length of visible dislocations. The main experimental bias leading to measurements uncertainties are the determination of the probed thickness and thus the volume, but also the impossibility to observe all dislocations at once. Indeed, due to the invisibility rule [20] only part of the dislocations are visible. Moreover, for dislocations located at grain boundaries and organized in walls, counting individual dislocations becomes rather difficult and inaccurate when they overlap/start overlapping. Dislocation counting on TEM or ECCI images in such a case is therefore a tedious task. To overcome this, a new methodology was recently developed based on ECCI imaging. A series of ECCI images are first recorded while rotating the sample, and then automatically analyzed through a clustering based algorithm, from which a dislocation density value is derived [21, 22].

EBSD is mostly used to characterize microstructures through orientation maps. Indeed, GND density is then computed from the local crystal curvature (through the local disorientation θ) and the map step size [7,13,23–25]. Although common, this approach is questionable. The uncertainty on the crystallographic orientations limits the sensitivity on GND densities, the resulting disorientation axis being significantly imprecise for low disorientation angles [26]. Weighed Burgers vector method proposes to consider a kind of Burgers circuit in order to reduce the imprecision at low disorientation angles [27], but only three components of the curvature tensor are considered and the contribution of elastic strain is also neglected. The latter is nevertheless a reasonable assumption in plastically deform metals [28,29], but not at slightly disoriented materials such as in GaN single crystals[29].

As a solution, the High (angular) Resolution EBSD (HR-EBSD) technique was developed under the impetus of Wilkinson et al. [30] and recently experienced a revival with the emergence of global image registration approaches [31–33], like the method used in this study [34,35]. All these methods apply

digital image correlation techniques to a pair of Kikuchi patterns in order to measure their relative displacement field with subpixel accuracy. Coupled with the precise knowledge of the projection geometry, relative lattice rotation and elastic strain can be captured with a typical accuracy of 10^{-4} (> 0.006°) in good experimental conditions. The Nye's tensor can then be calculated including the contribution of the elastic strains [36]. The complete determination of this tensor remains however limited by the two-dimensional nature of EBSD measurements, hence the growing interest in 3D HR-EBSD studies like in [37]. The higher accuracy of HR-EBSD techniques as compared to an indexing-based GND derivation comes with practical considerations limiting its wider use: use of a high-resolution camera with longer exposure time, large data collection (15 to 20 GB for the maps used in this article), each diffraction pattern being stored for the subsequent numerical intensive data post-processing. That is why identifying the cases of applications where the method brings a real improvement compared to indexing, in particular for deformed polycrystals, is crucial [34,38–40].

XRD is a more global measurement technique, that is often performed on a much larger volume, which in the present case will contain many grains of both phases with different orientations, and this different deformation behavior. The calculation of the dislocation density by X-Ray Diffraction (XRD) is based on the broadening of the diffraction peak, which seems more sensitive to SSD dislocation type [12]. Indeed, the calculation assumes the presence of 'crystallites domains' that would correspond to the cell/structure. Therefore, dislocations present at cells or grain boundaries would not be taken into account. This was experimentally confirmed by a direct comparison TEM / XRD measurements made on copper single crystals by Ungar et al [41].

Thus, the aim of this paper is (i) to present some quantitative measurements of dislocation densities performed with the same duplex steel samples using four different characterization techniques and for three different strain levels, (ii) to discuss the measurement uncertainties of all used techniques, and (iii) discuss the link between the obtained results and the different types of dislocation observed for each method.

2. Materials and methods

1) Materials

Observations were made on a commercial hot-rolled Outokumpo 2101 lean duplex stainless steel. This choice is motivated by the presence of two phases, austenite and ferrite, in which the dislocations adopt very distinct arrangements. Indeed, the dislocations appear straight with a high contrast and a variable thickness in the austenitic phase, which makes them easy to image. In the ferritic phase, on the contrary, the dislocations appear tortuous with a lower contrast, which makes them more difficult to image. It is therefore interesting to study the performance of measurement methods based on dislocation imaging (ECCI/TEM) for this material and more particularly the R-ECCI method.

The evolution of dislocation density was characterized in both ferritic and austenitic phases. Micro tensile samples (total length 112.5 mm, width 12.5 mm and a thickness of 1.5 mm) were deformed under an optical microscope using a Deben 2000E tensile stage. Using standard Digital Image Correlation (DIC) the deformation was determined on all points of the surface. One sample was deformed to 5% and the other one to 10%. In the present study, the austenite grain size will be impacted by the appearance of martensite in austenite during deformation.

For ECCI and HR-EBSD measurements, samples were mechanically ground, and the final polishing was performed using a 1 µm diamond solution. To avoid any strain hardening of the surface, a final electropolishing step was performed using A2 electrolyte (fromStruers APS, Denmark) at 20 V for 60 s with the Lectropol 5 device (Struers APS, Denmark).

To allow for TEM observations, the duplex samples were mechanically ground to obtain a thin sample of 50 µm thickness. Small discs of 3 mm diameter were subsequently extracted by punching and later electropolished using A2 electrolyte (from Struers APS, Denmark) with the Tenupol-5 device (Struers APS, Denmark). A final ion polishing step was performed using PIPS-II to increase the observable area with an acceleration voltage of 1.5 keV and angles of $\pm$ 4° for the ion beams for 2 hours.

For XRD measurements, samples were mechanically ground using SiC paper, down to a 1200P.

2) Methods

a) Transmission Electron Microscopy

TEM micrographs were acquired with a TEM JEOL 2100 LaB6 operating at 200kV. For dislocation densities measurements, the intercept method was used [42]. It consists in drawing lines of total length l on the image (arbitrary lines or regular grid) and counting the number of intersections n with dislocations. The dislocation density ρ is then calculated using the formula: $\rho = \frac{2n}{lt}$, with t the analyzed thickness. The determination of t was done by measuring the number of thickness fringes [43]. For a grain in a given two beam orientation, the probed depth z is proportional to the number of bands N observed and the extinction distance ξ_g related to the diffraction vector used: $z = \left(N - \frac{1}{2}\right) \xi_g$.

The observation of dislocations in TEM is possible in Weak Beam Dark Field (WBDF) mode [44] or in Bright Field (BF) mode. In both cases, it requires to orient the crystal in a Two-Beam (TB) [45] condition (only one diffracting vector $\overrightarrow{g_{hkl}}$). In these conditions, only screw dislocations with a burgers vector $\vec{b}$ respecting the relation $\overrightarrow{g_{hkl}}.\vec{b} \neq 0$ are visible, while the condition for edge dislocations is $\overrightarrow{g_{hkl}}.\vec{b} \times \vec{u} \neq 0$. As a result, for each orientation conditions, different dislocations might be invisible, and the density is

then always underestimated when determined from only one orientation condition. Therefore, for each strain rate and for each phase, two to three grains of each phase were oriented in several TB conditions.

b) R-Electron Channeling Contrast Imaging

SEM-ECCI observations were performed on a Zeiss Supra 55VP SEM with an accelerating voltage of 20 keV, a 120 µm diaphragm and a working distance close to 7 mm. The SEM images were recorded with a pixel size of 4.5 nm and a size of 1024 × 768 pixels.

BSE rotation images series were acquired following the procedure presented in [46] and [47]. For each pixel in the imaging series, the intensity variation as a function of the rotation angle can be plotted, it is called the Intensity Profile. The main intensity profile of a given grain is a signature of its crystallographic orientation[48]. For dislocation pixels, the intensity profile close to the rotation angle corresponding to a visibility condition will slightly differ from the one of the corresponding grains. A clustering algorithm, presented in [47] was developed to calculate the intensity difference between every pixel, and the mean intensity profile of each grain, so that the nature of each pixel could be identified: dislocation, matrix or noise. The dislocation density ρ_{clus} of a given area is then calculated using the general formula: $\rho_{clus} = \frac{L}{V}$, with L the dislocation length contained in the volume V. After data treatment, the total number of dislocation pixels N^{dislo} is determined. The total length of the dislocations is then calculated using

$$L^{dislo} = \frac{N^{dislo} \times P_S}{E}, \quad (2)$$

with E the mean thickness of dislocations (in pixels), and P_S the pixel size in nm. E is defined as

$$E = E^{app}/P_S, \quad (3)$$

with E^{app} the apparent dislocation width in nm, which is manually determined from the imaging series. The dislocation density rho is obtained by the relation:

$$\rho = \frac{N^{dislo} \times P_S}{S \times t \times E} = \frac{N^{dislo} \times {P_S}^2}{N^{tot} \times {P_S}^2 \times t \times E^{app}} = \frac{N^{dislo}}{N^{tot} \times t \times E^{app}}, \quad (4)$$

with *t* the analyzed sample thickness (in nm), and *S* the analyzed surface in nm². N^{tot} is the total number of pixels on each image series. Therefore, the dislocation density ρ only depends on E^{app} measured manually on the image, and on t the analyzed thickness. The value chosen for the interaction depth is $3\xi_g$ (approximately 93 nm for $\overrightarrow{g_{200}}$ in ferrite and 114 nm for $\overrightarrow{g_{220}}$ in austenite), in agreement with the predictions made by Zaefferer from ECCI simulations [49].

c) EBSD and High angular Resolution EBSD

EBSD was conducted with the same microscope as for the R-ECCI acquisitions. Electron BackScatter diffraction Patterns (EBSP) were acquired with an EBSD Symmetry camera (Oxford), an acceleration voltage of 15 kV, an exposure time of 32 ms, an aperture of 60 µm and a pixel size of 50 nm. The EBSP images were averaged by 3 to enhance their signal-to-noise ratio in view of the subsequent HR-EBSD analysis.

The latter is based on a global image registration approach implemented in ATEX-software [50] (developed at the University of Lorraine). EBSP are considered as a whole, through a unique and large region of interest, whose relative deformations are modelled by a linear homography [34]. Often used in computer vision to describe projections, the latter is measured by an iterative inverse-compositional Gauss Newton algorithm, modified to integrate a correction of optical distortions caused by camera lenses [51]. The reader is also referred to chapters 3 to 5 in [35] for all details.

The Nye's dislocation tensor is computed according to the Nye-Kröner theory [13,36]:

$$\boldsymbol{\alpha} = \mathbf{curl}\ \boldsymbol{\varepsilon} + \mathrm{tr}(\boldsymbol{\kappa_e}).\boldsymbol{I} - \boldsymbol{\kappa_e^T}, \tag{5}$$

where $\boldsymbol{\varepsilon}$ is the elastic strain tensor and $\boldsymbol{\kappa_e}$ the lattice curvatures. These curvatures can be approximated with a finite difference scheme:

$$\kappa_{ij} \cong {}^{\Delta w_i}/_{\Delta x_j}, \tag{6}$$

where Δw_i is the difference of rotation w_i (with respect to the axes of the basis) between two neighboring points separated spatially by Δx_j in the j-th direction. Thus, it arises the GND densities obtained by EBSD or HR-EBSD depend on the step size [52,53], which will be further discussed in this study.

Regarding the HR-EBSD technique, relative lattice rotations w_i between the reference and the target are directly obtained, as well as the elastic strains. In the case of standard EBSD, the contribution of elastic strains is unknown and simply omitted while the lattice rotations w_i are derived from the Euler angles [23]. Given two points "A" and "B" of the material, their respective orientation matrices $\boldsymbol{g_A}$ and $\boldsymbol{g_B}$ are computed and the disorientation angle $\Delta\theta$ is then deduced:

$$\Delta\theta = \min_k \left[\arccos\left(\frac{\mathrm{tr}(\boldsymbol{\Delta g}^k) - 1}{2}\right)\right], \tag{7}$$

where $\boldsymbol{\Delta g}^k$ is the "disorientation" matrix for the k-th symmetry of the crystal. This disorientation is decomposed into three rotations w_i with respect to the axes X_i of the sample frame:

$$w_i = -\, e_{ijk}.\Delta g_{ij} \cdot \frac{\Delta\theta}{2.\sin(\Delta\theta)}, \tag{8}$$

where e_{ijk} is the permutation symbol of Levi-Civita. The lattice rotations are evaluated considering the same reference point as in the HR-EBSD analysis. On the one hand, the location of this reference is not important from a strictly mathematical point of view, the calculation of the Nye tensor implying spatial derivatives. On the other hand, the grain internal disorientation angle is generally smaller between neighboring pixels. As mentioned in the introduction, this is detrimental to the accuracy on the disorientation axis [26], and the rotations w_i accordingly.

For both EBSD and HR-EBSD, only a partial computation of the Nye's dislocation tensor is possible. Indeed, the latter implies spatial derivatives along the surface normal direction ($\overrightarrow{X_3}$) which are unknown due to the two-dimensional nature of EBSD measurements:

$$\boldsymbol{\alpha} = \begin{bmatrix} \frac{\partial\varepsilon_{12}}{\partial x_3} - \frac{\partial\varepsilon_{13}}{\partial x_2} & \frac{\partial\varepsilon_{13}}{\partial x_1} - \frac{\partial\varepsilon_{11}}{\partial x_3} & \frac{\partial\varepsilon_{11}}{\partial x_2} - \frac{\partial\varepsilon_{12}}{\partial x_1} \\ \frac{\partial\varepsilon_{22}}{\partial x_3} - \frac{\partial\varepsilon_{23}}{\partial x_2} & \frac{\partial\varepsilon_{23}}{\partial x_1} - \frac{\partial\varepsilon_{21}}{\partial x_3} & \frac{\partial\varepsilon_{21}}{\partial x_2} - \frac{\partial\varepsilon_{22}}{\partial x_1} \\ \frac{\partial\varepsilon_{32}}{\partial x_3} - \frac{\partial\varepsilon_{33}}{\partial x_2} & \frac{\partial\varepsilon_{33}}{\partial x_1} - \frac{\partial\varepsilon_{31}}{\partial x_3} & \frac{\partial\varepsilon_{31}}{\partial x_2} - \frac{\partial\varepsilon_{32}}{\partial x_1} \end{bmatrix} + \begin{bmatrix} \frac{\partial w_{12}}{\partial x_3} + \frac{\partial w_{31}}{\partial x_2} & \frac{\partial w_{13}}{\partial x_1} & \frac{\partial w_{21}}{\partial x_1} \\ \frac{\partial w_{32}}{\partial x_2} & \frac{\partial w_{23}}{\partial x_1} + \frac{\partial w_{12}}{\partial x_3} & \frac{\partial w_{21}}{\partial x_2} \\ \frac{\partial w_{32}}{\partial x_3} & \frac{\partial w_{13}}{\partial x_3} & \frac{\partial w_{31}}{\partial x_2} + \frac{\partial w_{23}}{\partial x_1} \end{bmatrix}, \tag{9}$$

where

$$w_{ij} = -\, e_{ijk} w_k, \tag{10}$$

i.e.,

$$\begin{cases} w_1 = w_{32} = -w_{23} \\ w_2 = w_{13} = -w_{31}. \\ w_3 = w_{21} = -w_{12} \end{cases} \quad (11)$$

As a consequence, only α_{13}, α_{23} and α_{33} components are fully assessable [23–25]. The α_{12} and α_{21} components are determined by neglecting the contribution of elastic strains, which is partly unknown. Finally, the components α_{31} and α_{32} are not computable, neither the contribution of lattice curvatures nor that of elastic strains being fully assessable.

In this study, both EBSD and HR-EBSD results are discussed from the norm of the estimated Nye's tensor. Its α_{ij} components having units of inverse length, there are divided by the norm b of the Burgers vector to express a GND density in m^{-2}:

$$\rho_{GND} = \frac{1}{b}\sqrt{\alpha_{ij}.\alpha_{ij}}. \quad (12)$$

d) X-Ray Diffraction

XRD experiments were conducted in a BRUKER D8 advance diffractometer equipped with a Mo-Kα radiation ($\lambda_{K\alpha 1} = 0.7093$ Å), a Zr filter to absorb the K_β radiation from molybdenum, a 1 mm collimator and a Lynxeye linear detector. The goniometer is operating in a θ/θ configuration: the X-ray tube and the detector present symmetrical movements while the sample remains horizontal in a fixed central location. Estimation of the crystallite size, D, as well as the microstrain, RMS (Root Mean Square), was obtained by XRD line broadening using Popa model integrating in Maud software.

XRD diagrams were fitted with a pseudo-Voigt function in Maud software [54]. Instrumental parameters for the fit (Caglioti parameters, Lorentzian/gaussian ratio) were determined on a standard NIST powder of hexaboride of lanthanum (LaB_6). The formula proposed by Murugesan *et al.* [55] for the dislocation density calculation was used.

The ρ dislocation density can be decomposed into two contributions:

$$\rho = (\rho_D \times \rho_S)^{1/2} \quad (13)$$

with ρ_D the domain contribution $\rho_D = \frac{3}{D^2}$ and ρ_S the deformation contribution $\rho_S = \frac{k\langle\varepsilon_L^2\rangle}{b^2} = \frac{k\langle\varepsilon_L^2\rangle\sqrt{2}}{a^2}$

with k the material constant, D the crystallite size, $\langle\varepsilon_L^2\rangle$ RMS micro strain and b the burger vector (here $b = \frac{a}{\sqrt{2}}$). All uncertainties were calculated from the formulas given by Murugesan *et al*.[56]

3. Results

1) Transmission Electron Microscopy

For each strain rate and for each phase, two to three grains of each phase were orientated in several TB conditions. All g_{hkl} diffracting vectors used for the analysis are listed in Table 1. The acquisition of dislocation images on the 10% deformed sample was difficult due to the strong disorientation present in the grains (about 5 to 6° for the most disoriented areas), and fewer diffraction conditions were observed for that sample. To limit the underestimation, the dislocation density for each grain was chosen as the maximum one measured on the different orientation conditions.

Table 1 : Summary of diffraction vectors used to characterize the three austenite grains and three ferrite grains, for different strain rates.

	Austenite			Ferrite		
	Sample 1 0%	Sample 2 5%	Sample 3 10%	Sample 1 0%	Sample 2 5%	Sample 3 10%
Diffracting vectors	$(1\bar{1}1)$ $(\bar{2}20)$ (311)	$(1\bar{1}1)$ (110)	$(1\bar{1}1)$	(101) $(1\bar{1}0)$ $(1\bar{1}2)$	$(01\bar{1})$ (100) $(\bar{2}1\bar{1})$	(110) $(2\bar{1}1)$
Diffracting vectors	$(1\bar{1}1)$	(110) $(11\bar{1})$	(110)	$(\bar{1}10)$ $(0\bar{2}0)$	(110)	(110)
Diffracting vectors	(202) $(1\bar{1}\bar{1})$	$(1\bar{1}1)$ $(\bar{1}10)$ (311)	$(11\bar{1})$	$(01\bar{1})$		

The analyzed area slightly varies for the different samples. For 5% and 10% deformed grains, the average image area is respectively 0.5 μm^2 and 0.3 μm^2, while it is 3.5 μm^2 for the undeformed sample. Indeed, for high deformation levels, disorientation within each grain increases. Therefore, contrasts conditions vary rapidly and the observable areas on each image are reduced. Moreover, with increasing dislocation densities, dislocations overlapping increases. It was then necessary to enhance the magnification in order to have sufficient resolution to distinguish them from each other.

Figure 1 shows typical TB TEM micrographs obtained in austenite and in ferrite for undeformed and deformed samples at 5 and 10%. The dislocations appear in black on a white background.

In the undeformed state, only few dislocations are seen in the austenite in Figure 1(a). The density seems higher in ferrite (Figure 1(b)) where dislocations appear as points or lines which reveals that their orientation in the grain is random. After 5% deformation, the number of visible dislocations has greatly increased. In Figure 1(d), the dislocations in the 5% deformed ferrite have clustered and become more tortuous. The overlapping of dislocations is important, as in the deformed austenite (Figure 1(c)). In the case of the 10% deformed sample (Figure 1 (e) and (f)), it is quite difficult to image dislocations over large surfaces, because the important disorientation locally modifies the contrast conditions. However, there is not much difference in the resulting micrographs, compared to the 5% deformed sample. It is necessary to remind that the local thickness of the diverse thin foil is quite different. For example, for the deformed ferrite at 5% it was measured to be 220 ± 37 nm , while it is 146 ± 37 nm for the 10% deformed sample (Figure 1 (d) and (f)). This can be misleading for a direct eye comparison of the images.

Dislocation densities were determined using the intercept method. The maximum values for each deformation level and phase are presented in table 2.

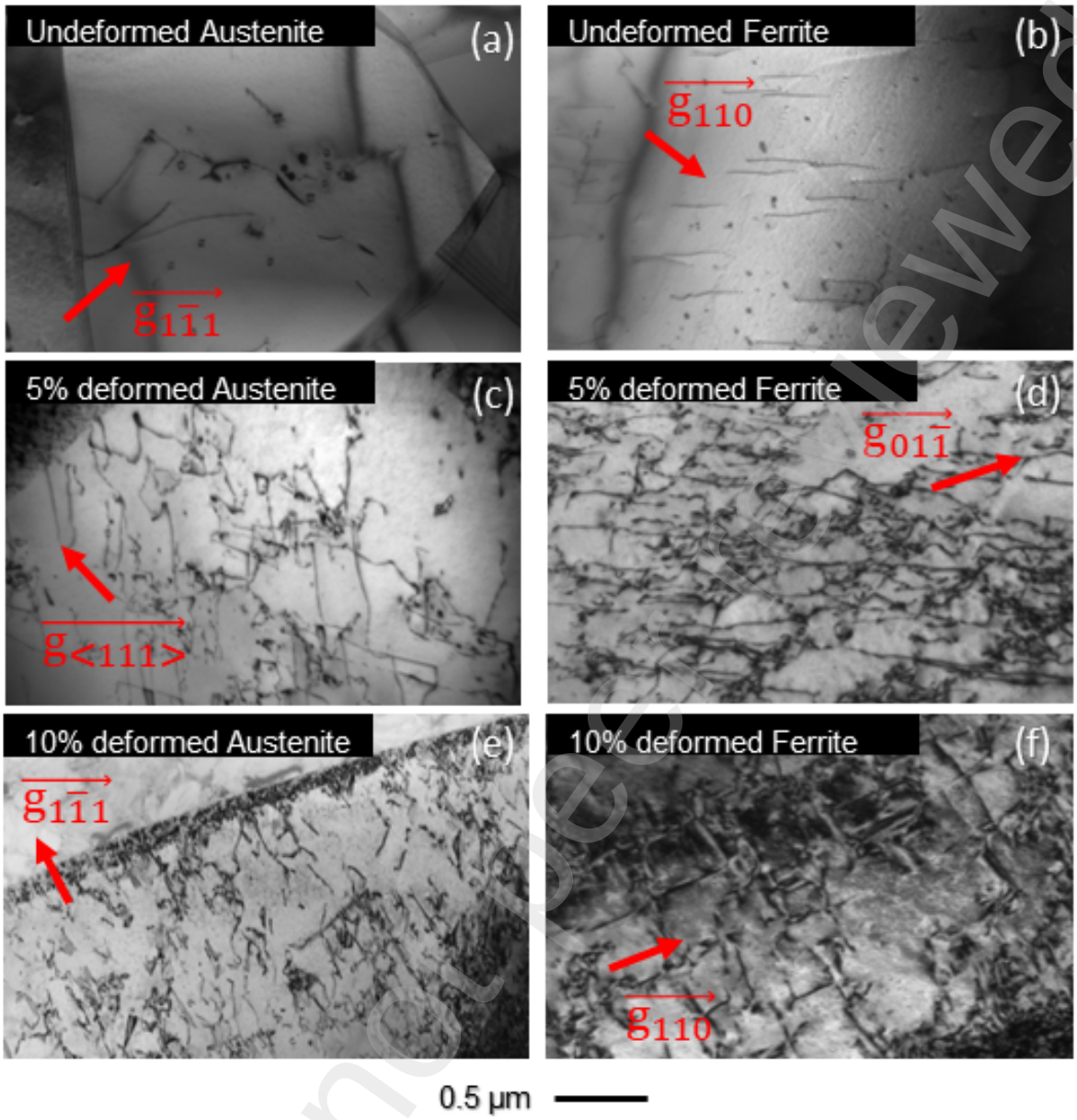

Figure 1: TEM image acquired on different grains. For each image, the dislocation lines are visible in black on a white background. (a) Undeformed austenite grain. (b) Austenite grain in sample deformed at 5%. (c) Austenite grain in sample deformed at 10%. (d) Undeformed ferrite grain. (e) Ferrite grain in sample deformed at 5%. (f) Ferrite grain in sample deformed at 10%.

Table 2 : Mean value of the dislocation density (m^{-2}) obtained on ferrite and austenite grains for different strain rates

	0%	5%	10%
Austenite	$(1.1 \pm 0.1) \times 10^{13}$	$(6.7 \pm 1.0) \times 10^{13}$	$(1.4 \pm 0.3) \times 10^{14}$
Ferrite	$(1.2 \pm 0.1) \times 10^{13}$	$(5.7 \pm 0.8) \times 10^{13}$	$(1.2 \pm 0.2) \times 10^{14}$

The dislocation density is measured to be similar in both phases. As expected, the dislocation density increases with deformation, with a slightly quicker increase in austenite compared to ferrite, as austenite deforms before ferrite [57]. After 10% deformation, dislocation densities measured in ferrite

and in austenite are about 10 times higher than before deformation. However, in the 10% deformed sample, it is very hard to observe the dislocations on a large surface on a single image because of the deformation but also because of the thin foil which is slightly twisted. This adds to the difficulty of observing the dislocations but also to the measurement, especially on the top of the image of the 10% deformed ferrite (Figure 1(f)). This is why the measurement uncertainty increases for the latter values as it becomes problematic to distinguish dislocations from each other, due to the overlapping of dislocations and the rapidly changing observation conditions, but also due to the uncertainty of the volume which may lack accuracy.

2) R-ECCI and Clustering

The ECCI allows the observation of dislocations in white on a black background. In the received state, Figure 2(a and b), the dislocations appear as straight lines or as dots, indicating it is rather parallel or perpendicular to the surface. Moreover, at first sight, there would be more dislocations in the ferrite on the ECCI images (Figure 2(b)) than in the TEM images (Figure 1 (b)) which could be due to the thinner thickness observed on the TEM images. In austenite, after deformation, the dislocations appear as straight lines and are mainly aligned along {111} planes, Figure 2(c) and (e). The high concentration of dislocations in the 10% deformed austenite (Figure 2(e), blue arrow) results in a large variation in contrast, especially at the grain boundaries, making it difficult to detect dislocations using the clustering algorithm. In the case of ferrite Figure 2 (b, d and f), the dislocations are more tortuous and seem to have random directions including in the deformed cases Figure 2 (d and f). Moreover, the contrast variations are already visible after 5% in the deformed ferrite Figure 2 (d) and become even more significant after 10% deformation (red arrow).

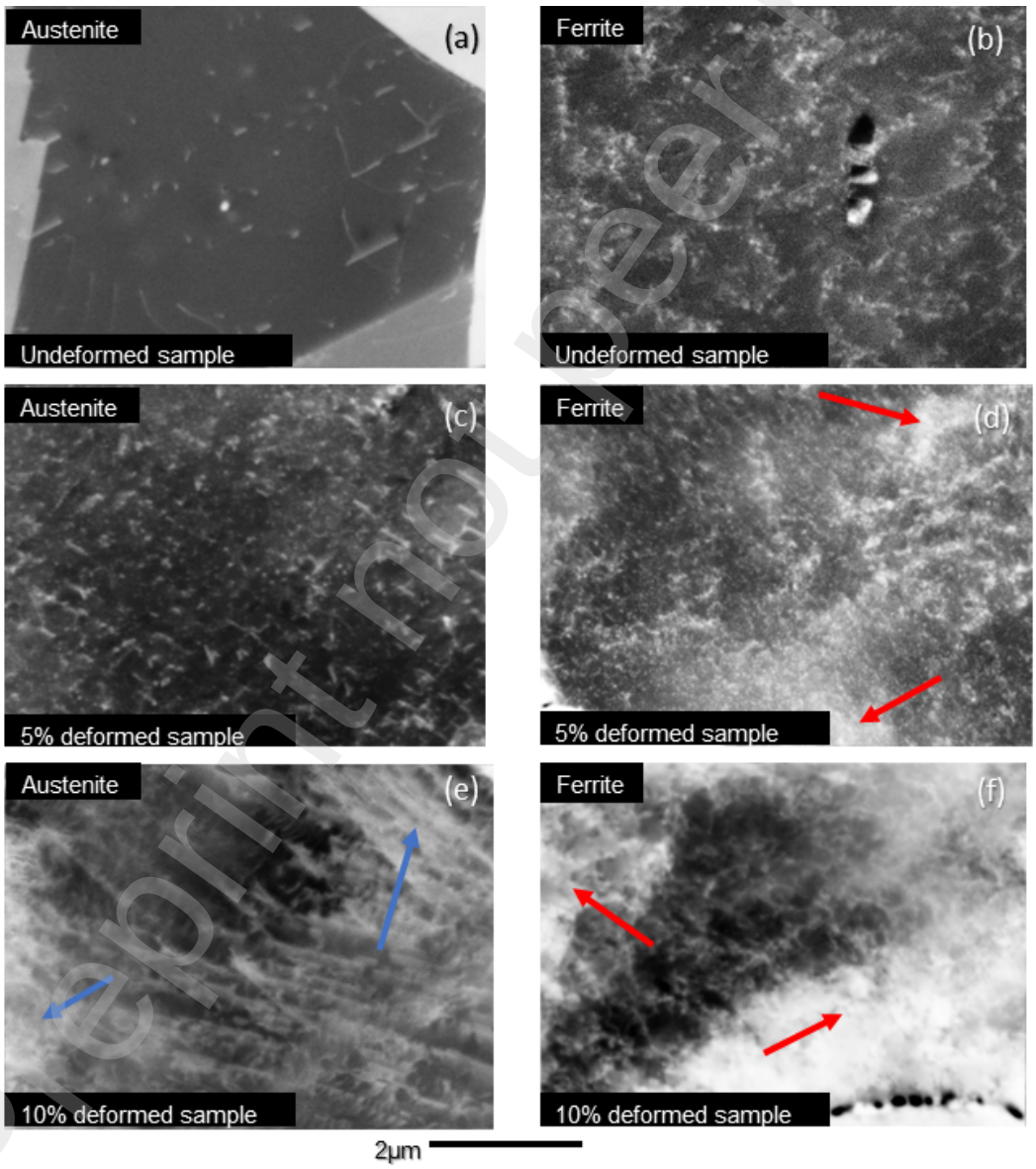

Figure 2: BSE image acquired with an accelerating voltage of 20 keV, aperture of 120 µm and pixel size of 4.5 nm. (a), (c) and (e) show respectively three austenite grains present in an undeformed, 5% deformed and a last 10% deformed sample. Similarly, images (b), (d) and (f) show respectively three ferrite grains present in an undeformed, 5% deformed and a last 10% deformed sample.

After analysis, detected dislocations are represented as green pixels on a dark matrix, Figure 3 (b), (d) and (f) for the undeformed, 5 %, and 10% deformed sample respectively. The dislocation density calculated by the clustering algorithm is $(1.5 \pm 0.1) \times 10^{13}\ \mathrm{m}^{-2}$ for undeformed austenite (Figure 3 (a) and (b)) for which almost all dislocations were detected. This first case illustrates the effectiveness of the algorithm when the dislocations are well distinct and show a good contrast with the grain. In the case of ferrite after 5% deformation, the BSE image in Figure 3 (c) shows more clustered dislocations that are harder to distinguish (blue circle). In that area, some dislocations are not indexed by the algorithm, Figure 3 (d), and a local underestimation of the density is expected. Moreover, in some other area, the large amount of dislocation creates local disorientation that affects the contrast (yellow arrows). After analysis, those areas appear as large cluster (yellow arrows) much thicker than what they should be compared to the apparent width of the dislocations (Figure 3 (c)). This probably leads to a local over's estimation of the density. As a result, for this ferrite grain, the density was measured to be $(5.6 \pm 1.0)\ 10^{13}\ \mathrm{m}^{-2}$.

Finally, an austenitic grain subjected to 10% strain is displayed in Figure 3(e). This grain is highly disoriented, resulting in significant contrast variations in the grain (red arrows). Although the dislocations present in austenite are easier to image in ECCI than in ferrite, austenite deforms before ferrite, so that dislocation densities quickly reach values that are no longer measurable by clustering. Indeed, the dislocations form cells and become difficult to distinguish from each other. As with the previous ferritic grain, the clustering algorithm finds areas where all dislocations are merged (yellow arrows on Figure 3(f)), which gives an overestimation of the density. These "large clusters" are partly due to the strong contrast variation but also to the proximity or overlapping of the dislocations. Moreover, for some areas there is an information loss (blue circles). For this sample, the clustering is more efficient in the center of the image than on the edges because of the more important disorientation at the grain boundaries. For all those reasons, the obtained value of $(7.4 \pm 1.5) \times 10^{13}\ \mathrm{m}^{-2}$ seems underestimated. In that case, and for comparison's sake, single ECCI images were used and dislocations density were measured manually. The measured density for the 10% deformed austenite is $(1.3 \pm 0.4) \times 10^{14}\ \mathrm{m}^{-2}$, which confirms that it is well beyond the current limits of the method.

Table 3 : Mean value of the dislocation density (m^{-2}) obtained on ferrite and austenite grains for different strain rates measured from ECCI imaging.

	0%	5%	10%
Austenite	$(1.5 \pm 0.1) \times 10^{13}$	$(4.5 \pm 1.0) \times 10^{13}$	$(7.4 \pm 1.5) \times 10^{13}$
Ferrite	$(2.5 \pm 0.1) \times 10^{13}$	$(5.6 \pm 1) \times 10^{13}$	$(5.4 \pm 1) \times 10^{13}$

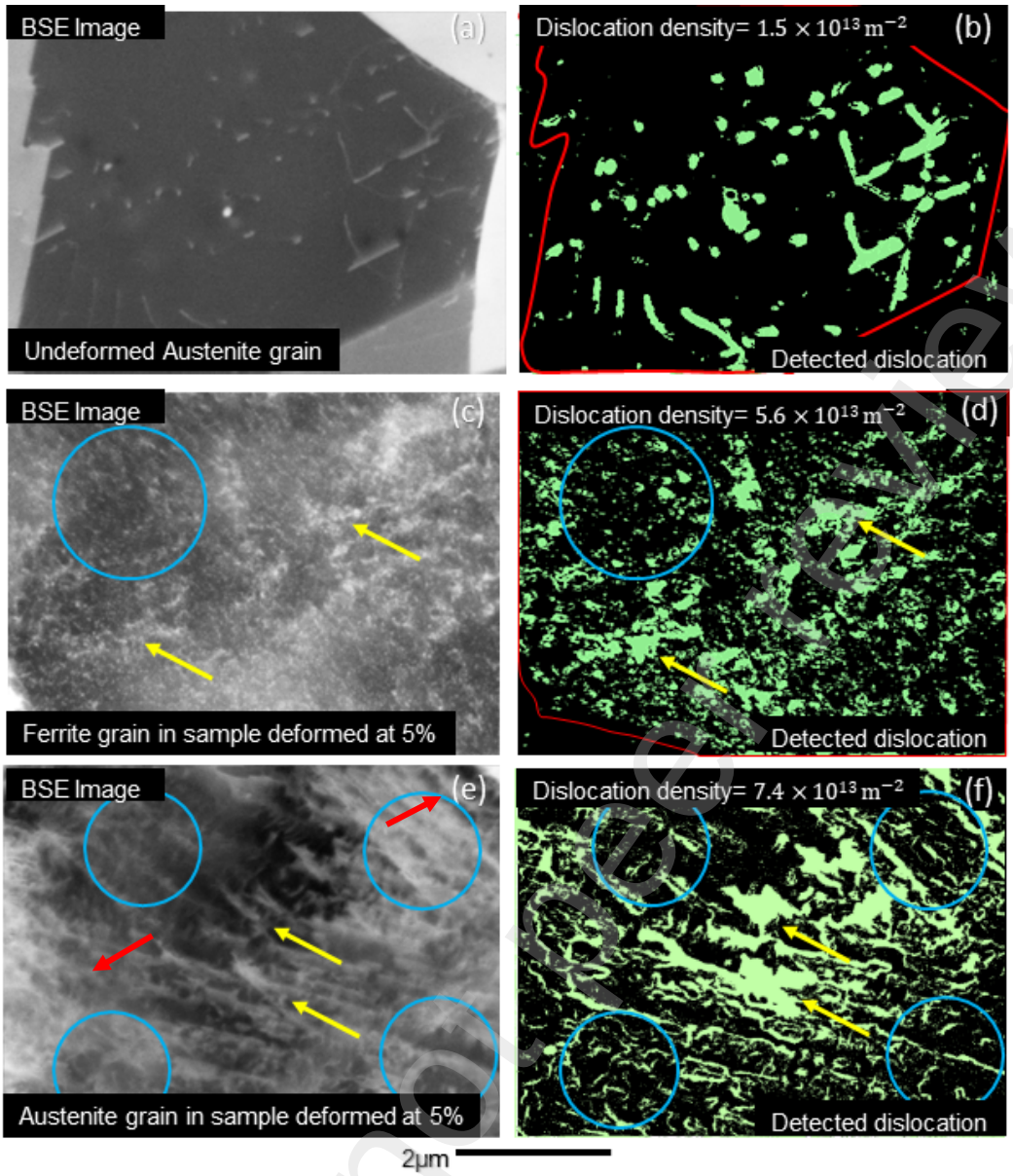

Figure 3: BSE image acquired with an acceleration voltage of 20 keV, an aperture of 120 µm and a pixel size of 4.5 nm. (a), (c) and (e) show respectively an undeformed austenite grain (a), a ferrite grain present in a sample deformed at 5% (c) and an austenite grain present in a sample deformed at 10% (e) The images (b), (d) and (f) show the results obtained by the clustering algorithm where the detected dislocations appear in green and the densities thus measured on the grains (a), (c) and (e) respectively. Only the pixels in the red box (b) and (d) were considered for the calculation of the dislocation densities. The blue circles show the areas where information was lost and all dislocations are not or partially detected. The yellow arrows show the areas where dislocations are detected but much thicker than in the BSE images.

3) Electron Back Scattered Diffraction

Several EBSD acquisitions were carried out for each strain rate. The areas chosen usually covered both phases and contain interfaces or grain boundaries, where deformation is known to localize for this type of alloys. Note that the investigated areas are rather small (5×5 µm maximum). Acquisition time was indeed limited to around 23 min per map, since the high sensitivity of the HR-EBSD technique can make image drift becoming visible for longer acquisitions.

In a first time, orientation mappings are post-processed in a standard way by assessing the norm of the Nye tensor from Euler angles. The so-obtained GND density maps are shown in Figure 4, bottom row, and they will be further discussed in the light of HR-EBSD measurements.

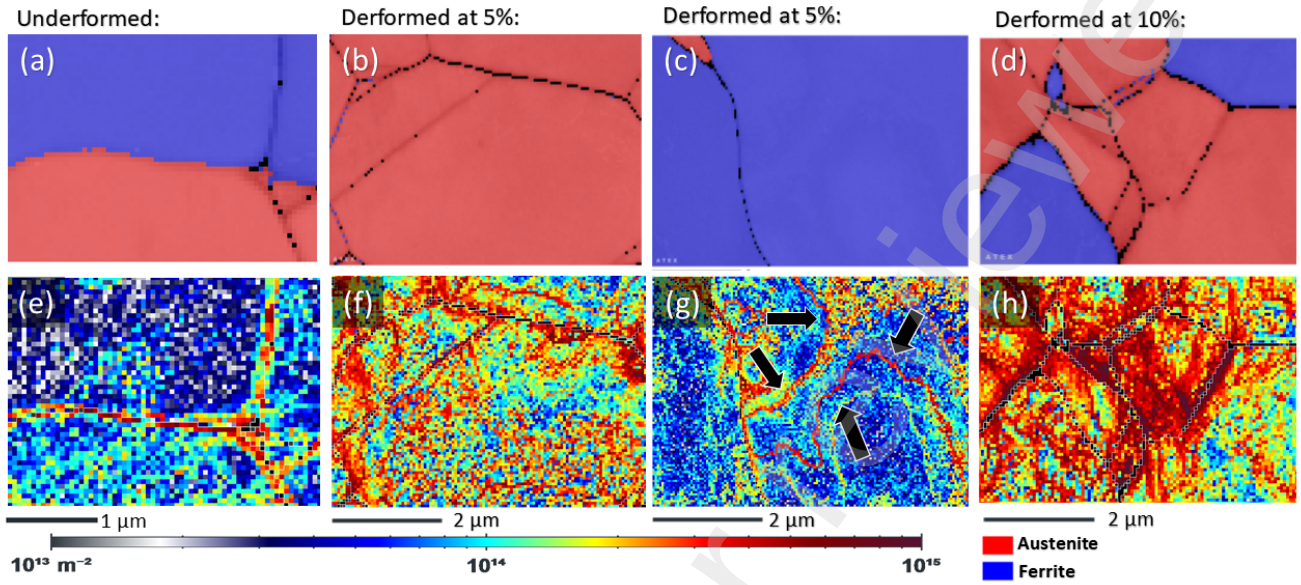

Figure 4: Example of EBSD phase maps (top line, with austenite in red and ferrite in blue) obtained on undeformed, 5 and 10% deformed steel samples. Norm of Nye tensor map obtained by EBSD (bottom line).

To obtain a dislocation density value which can be compared with the other used methods, average values were calculated, for each present grain, and given in **Table 4**. With increasing strain, the density in austenite (red in Figure 4, top row) evolves faster than that contained in ferrite (blue), which is consistent with the fact that austenite deforms before ferrite [57].

Table 4: Average value of the dislocation density (m^{-2}) obtained with the norm of Nye tensor, on ferrite and austenite grains for different strain rates

	0%	5%	10%
Austenite	$(1.2 \pm 0.7) \times 10^{14}$	$(2.1 \pm 0.8) \times 10^{14}$	$(3.3 \pm 1.2) \times 10^{14}$
Ferrite	$(4.6 \pm 1.4) \times 10^{13}$	$(1.1 \pm 0.5) \times 10^{14}$	$(2.1 \pm 0.9) \times 10^{13}$

4) High Resolution-Electron Back Scattered Diffraction

An HR-EBSD analysis is now conducted on each one of the previous EBSD data sets. The strain concentration at the grain boundaries for both phases is now more clearly observed from the GND mappings in Figure 5.

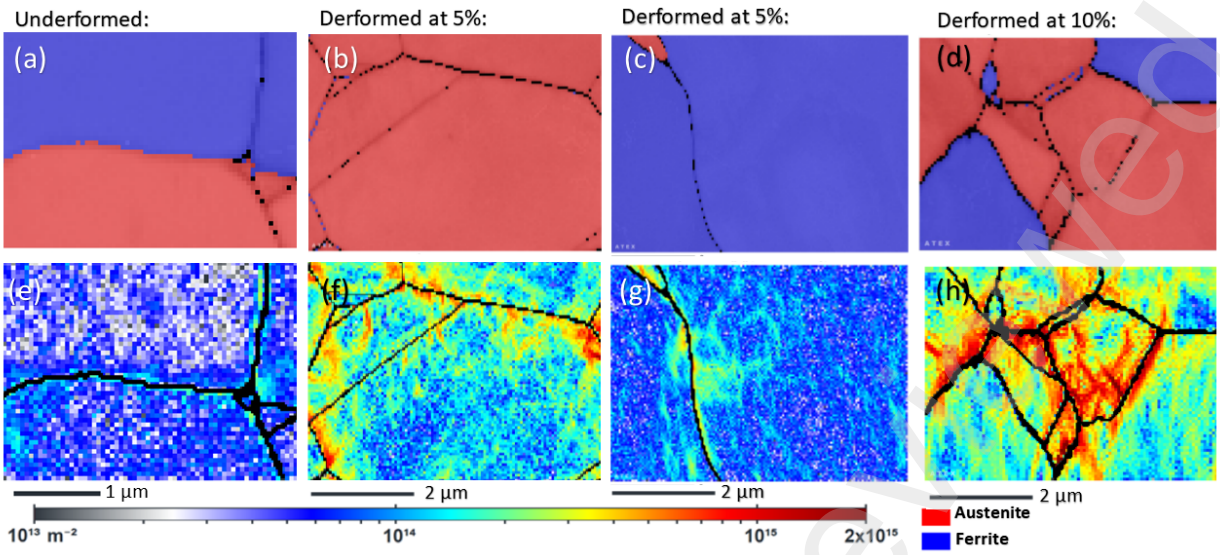

Figure 5: Example of EBSD map (top line) obtained on undeformed, 5 and 10% deformed steel samples. GND-map obtained by HR-EBSD (bottom line).

Same as for EBSD, the dislocation density is averaged at the grain scale and values are summarized in Table 5. Overall, both the EBSD and the HR-EBSD techniques are quite in agreement, but the average GND density obtained by EBSD is always higher than with HR-EBSD. This is attributed to the noisier character of the maps derived in Euler angles (Figure 4), while the measurement uncertainty is estimated at $1.1 \times 10^{13}\ \mathrm{m}^{-2}$ with HR-EBSD (minimum of GND obtained).

This is particularly visible in Figure 4g, where the continuous red lines (spotted with back arrows) do not correspond to any obvious dislocation structure, that the sensitivity of the HR-EBSD technique on orientation changes would have detected in Figure 5g. This is also confirmed by the absence of such marked features in the virtual backscatter electron diode image in Figure 6(a) either, although its contrast is very sensitive to orientation changes as well (see [34] for more details). Note that it only provides qualitative information whereas the HR-EBSD technique is quantitative.

The aforementioned red lines in Figure 4g come from a discretization of orientations by the indexing software. Indeed, they superimpose with the relative rotation w_2 within grain derived from Euler angles in Figure 6(b), which locally presents discontinuities of the order of 0.2°, in agreement with the angular resolution of the indexing techniques. Note that the considered axis is here parallel to the image height, but its choice is not relevant for the purpose. Point is to underline that knowledge of the disorientation axis is essential for the accurate assessment of GND densities (since a tensor is to be computed). That is why those artifacts are less visible from the disorientation angle in practice (not shown here), since the latter does not carry information about the axis.

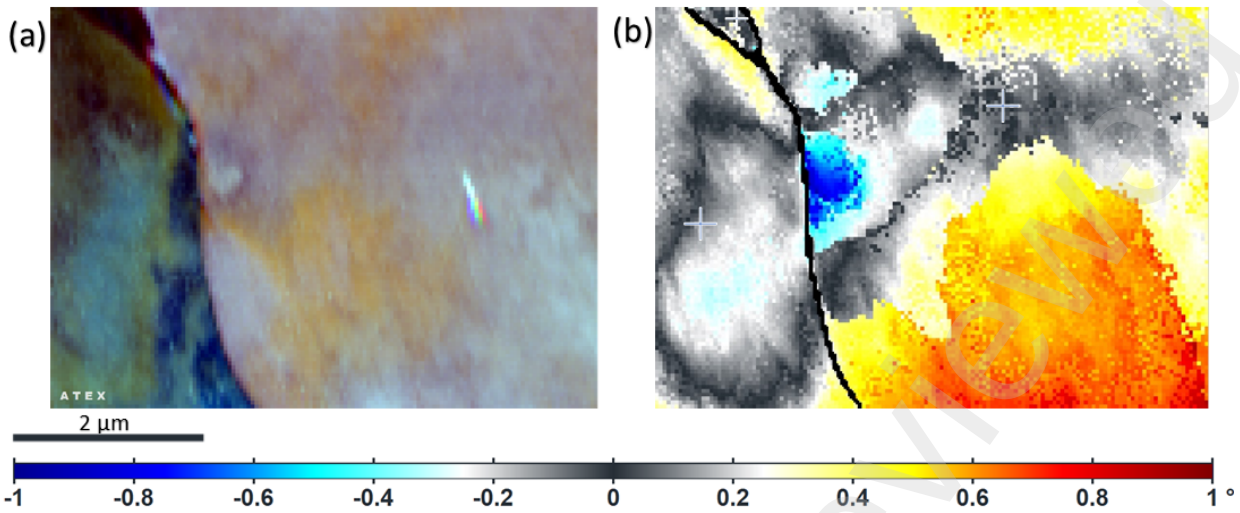

Figure 6: (a) Virtual forescatter electron diode image computed form the Kikuchi patterns stored for the HR-EBSD analysis. (b) Relative rotation around the second axis of the sample frame. These rotations are computed from Euler angles, relatively to a reference point within each grain (spotted by a white cross).

Note that the largest discrepancy between EBSD and HR-EBSD is observed at 0% strain in austenite, where the value obtained by EBSD is twice higher than the one obtained by HR-EBSD. Although such a gap is not observed in ferrite, it is not surprising it concerns the sample with the lowest grain internal disorientations. As already mentioned, uncertainty on the disorientation axis derived from Euler angles is maximal.

Table 5: Average value of the dislocation density (m^{-2}) obtained using of HR-EBSD on ferrite and austenite grains for different strain rates.

	0%	5%	10%
Austenite	$(5.6 \pm 1.1) \times 10^{13}$	$(1.7 \pm 0.2) \times 10^{14}$	$(2.6 \pm 0.2) \times 10^{14}$
Ferrite	$(4.2 \pm 1.1) \times 10^{13}$	$(8.6 \pm 1.5) \times 10^{13}$	$(1.9 \pm 0.2) \times 10^{14}$

Overall, the average GND density obtained by HR-EBSD follows the same trends than with EBSD. Between the undeformed sample and the 5% deformed sample, the dislocation density in Ferrite increases by a factor of 2 whereas in austenite the evolution is 3 times faster. This slower increase in ferrite for the first stages of the deformation is consistent with the fact that Austenite is deforming first. However, between the 5% deformed stage and the 10% deformed stage, the austenite keeps increasing but at a slower rate than in the previous stage (from a factor of 3 to 1.5) while dislocation density in ferrite has a slightly higher factor and increases from 2 to 2.2.

5) X-Ray Diffraction

XRD diffractogram obtained for 0%, 5% and 10% deformed samples are presented on **Figure 7**.

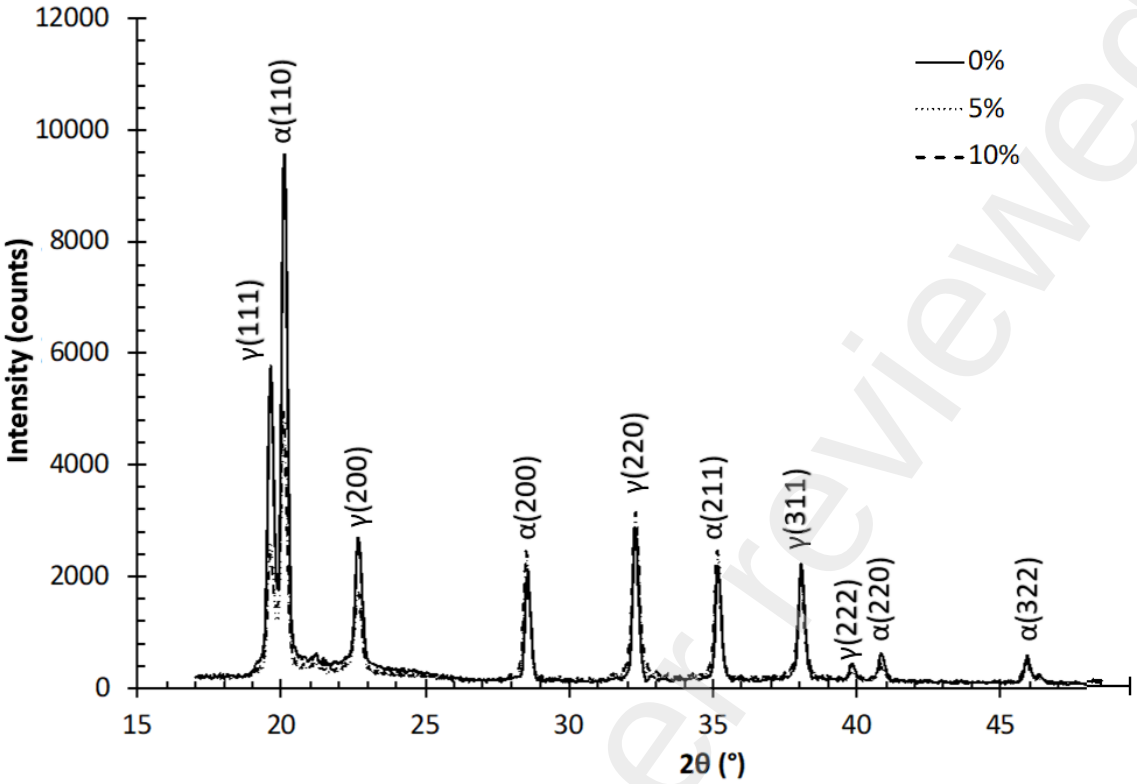

Figure 7: Experimental XRD diffractograms for 0%, 5% and 10% deformed samples.

Density dislocation obtained on ferrite and austenite grains for different strain rates are summarized on the table 6.

Table 6: Average value of the dislocation density (m^{-2}) obtained thanks to XRD on ferrite and austenite grains for different strain rates.

	0%	5%	10%
Austenite	$(4.0 \pm 10.7) \times 10^{13}$	$(1.7 \pm 0.3) \times 10^{14}$	$(1.8 \pm 0.3) \times 10^{14}$
Ferrite	$(6.1 \pm 13.1) \times 10^{13}$	$(7.6 \pm 4.6) \times 10^{13}$	$(9.0 \pm 2.6) \times 10^{13}$

The measurement uncertainties on the undeformed sample are on the order of 200%. This is because the RMS microstrain $\langle \varepsilon_L^2 \rangle$ is included in the curve fitting parameters and is difficult to obtain accurately on the undeformed sample. In the deformed sample, RMS microstrain $\langle \varepsilon_L^2 \rangle$ is higher and can be more precisely determined. Thus, its uncertainty drops by a factor of 10, and the global measurement uncertainty is then three to four times smaller.

During deformation, the dislocation density present in the austenite measured by XRD increases faster than the density present in the ferrite, which is consistent with the deformation mechanism of a duplex steel [57]. For instance, the density in austenite is measured to be twice higher than in ferrite after 5% and 10% of deformation. After 10% of deformation, the density does not evolve much compared to 5% deformation, for both phases. For austenite phase, it was observed that the austenite grains were partly transformed into martensite. Thus, the crystallite size D was overestimated in this sample and therefore the dislocation density present in the 10% deformed sample may be underestimated.

4. Discussion

All methods presented here do not measure the same type of dislocation (ρ_c , ρ_w ,ρ_{GB}). Moreover, each method has its own limitations and uncertainties so it is important to compare them carefully.

Each used measurement method relies on different computational means, based on diffraction, disorientation, channeling contrast or manual dislocation counting. Figure 8(a) shows a schematic representation of the dislocation configuration that can be observed within one grain (group of random dislocations ρ_c, dislocation cell ρ_w, dislocations grouped at the grain boundary ρ_{GB}).

XRD measurements allow to measure disorientations, within what is defined as crystallites, Figure 8(b). This means that the dislocations close to the grain boundaries (ρ_{GB}) or grouped in cells (ρ_w) which are the main source of GND will not be considered when calculating the dislocation density. Moreover, a crystallite is defined as an area showing a low disorientation, it can be a grain, but also a dislocation cell. Therefore, dislocation cells will be observed as grain with this method. The size of crystallite is often very complicated to obtain [58] because it can vary enormously from case to case and it becomes difficult to calculate it precisely if the shape of the crystallite [59] or if the deformation [60] becomes anisotropic.

In the case of TEM and ECCI imaging methods, dislocations are theoretically all visible but it is often very difficult to distinguish dislocations near grain boundaries as the disorientation is important and the conditions for observing dislocations change rapidly, Figure 8(c). Moreover, imaging methods give images projected on a surface and overlapping dislocations, such as at the ones present at grain boundary or at cell walls, cause a non-negligible uncertainty [47]. This is why the densities measured by imaging can be considered to be mainly dislocations isolated from the dislocation clusters (ρ_c).

In the case of the EBSD or HR-EBSD methods presented Figure 8(d), the relative rotation and elastic strain fields are measured from which a GND dislocation density is derived. The most influential parameter on the results is the pixel size used. As shown by Jiang *et al.* [52] the dislocation density can vary by an order of magnitude when the pixel size is doubled. Indeed, if the maps are acquired with a very fine step, as on the Figure 8(d) (left) then the dislocations will be discernible and will be defined as GND's. However, if a larger step is used (as in the Figure 8(d) right), some dislocation clusters could have their Burgers vector opposed and no longer cause lattice rotation. These dislocations will then be considered as SSDs. As specified by Jiang *et al.* [52], these variation in measured density are the consequence of a change in the threshold defined between SSDs and GNDs.

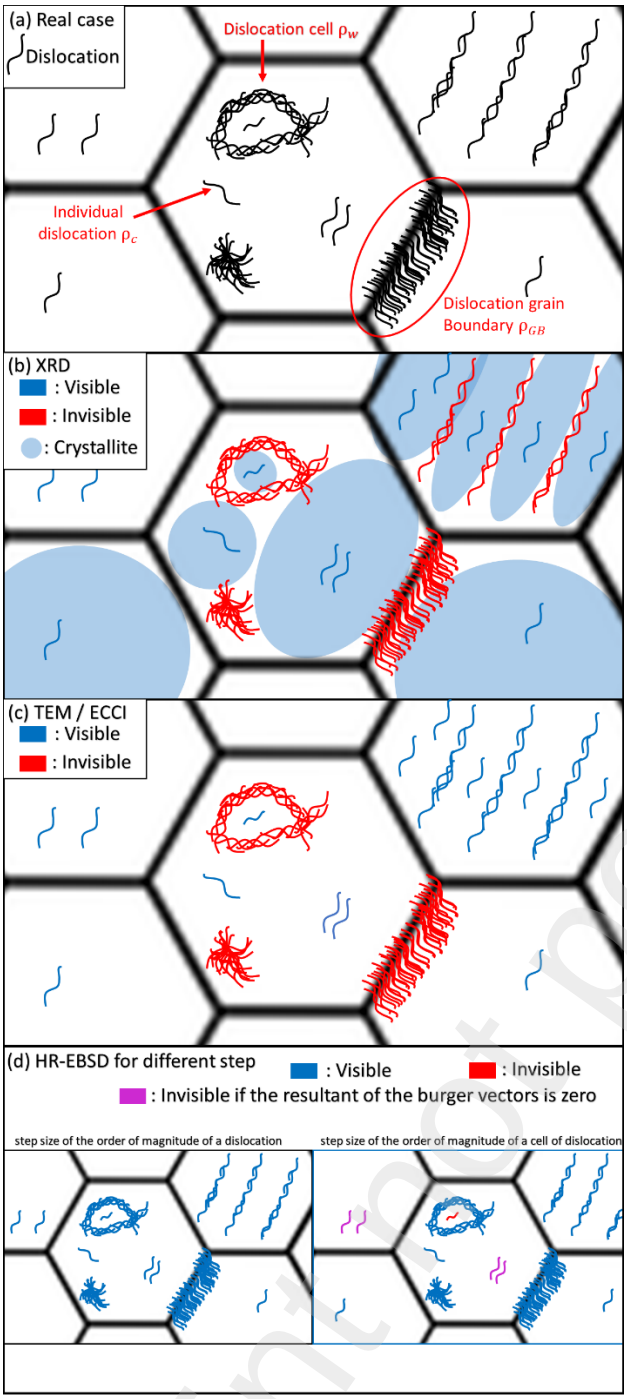

Figure 8: Grain pattern with several cases of dislocations observable: dislocation cluster, isolated dislocation, dislocation cell, dislocation cluster present in particular planes. (a) Real case, (b) Illustration of dislocations analyzed by XRD and the crystallite size used. (c) Illustration of dislocations analyzed by TEM/ECCI imaging methods. (d) Two cases illustrating what the HR-EBSD method can distinguish according to the pixel size used (very fine pixel size on the left and a larger pixel size on the right).

The quantitative comparison of all measurements results is presented on Figure9. The values obtained for the 0% sample remain in the same order of magnitude regardless of the method, although XRD measurement uncertainty is very high (270.9%, calculated with the method of Murugesan *et al.* [56]).

After 5% of deformation, a higher dislocation density is expected in austenite compared to ferrite. XRD and HR-EBSD results are close to each other and both indicate dislocation density twice higher in austenite than in ferrite for this state (around $1.7 \times 10^{14}\ \mathrm{m}^{-2}$ and $0.7 \times 10^{14}\ \mathrm{m}^{-2}$ respectively).

However, imaging-based measurements such as ECCI and TEM indicate smaller densities with around $5 \times 10^{13}\,\mathrm{m}^{-2}$, for both phases. In austenite, where the dislocation density evolves faster during the deformation, the imaging methods ECCI and TEM give underestimated measurements due to the overlapping of dislocations.

For the 10% deformed sample, ECCI measurement were not possible as the density is over the acceptable measurement range. All other three methods reveal a large increase in dislocation density. HR-EBSD gives the highest dislocation density with $(2.6 \pm 0.2) \times 10^{14}\,\mathrm{m}^{-2}$ for austenite and $(1.9 \pm 0.2) \times 10^{14}\mathrm{m}^{-2}$ for ferrite. However, the results from TEM imaging indicate a similar density for both phases with $(1.2 \pm 0.2) \times 10^{14}\mathrm{m}^{-2}$ for ferrite and $(1.4 \pm 0.3) \times 10^{14}\mathrm{m}^{-2}$ for austenite. Finally, XRD measurements, are different for both phases with $(9.0 \pm 2.6) \times 10^{13}\mathrm{m}^{-2}$ for ferrite and $(1.8 \pm 0.3) \times 10^{14}\mathrm{m}^{-2}$ for austenite. Those values are very close to that measured in the 5% deformed sample, which is quite surprising as the dislocation is expected to increase between those two states.

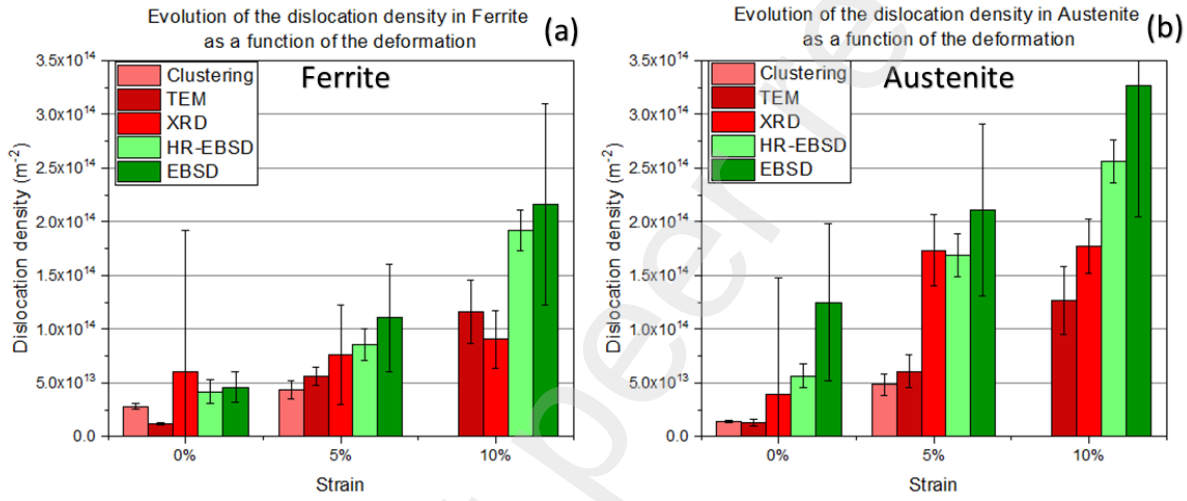

Figure 9: Comparison of dislocations densities measured with XRD, TEM, HR-EBSD, and R-ECCI for (a) austenite and (b) ferrite, in the undeformed, 5% and 10% deformed samples.

We should note that TEM, ECCI-based and EBSD/HR-EBSD are all local measurement techniques, that will provide data on a limited number of grains. In a polycrystalline material, the deformation process of individuals grains is dependent on their relative orientation to the loading geometry and on their relative neighborhood.

1) SSD measurement (TEM; ECCI and XRD)

Both ECCI and TEM observations provide a majority determination of the SSD dislocation density. Indeed, imaging methods lose a lot of information due to dislocation overlapping [47], as is observed at grain boundaries and in dislocation cells. In practice, these methods are applied at the center of the grain (relatively far from ρ_{GB}) and cannot accurately measure the number of dislocations in cells or walls (ρ_w). Even if it is difficult to know how far the dislocations generated at the grain boundaries by the deformation will disperse inside the grain [61] we consider that all observations were performed inside the grains, and do not take into account the dislocations at grain boundaries. Moreover, both methods are very local. For all those reasons one can expect similar measurements from both techniques, which is the case, considering the uncertainty of both measurements. However, we observed that for higher

dislocation densities, and specifically for the 10% deformed sample, the disorientation within the grains, and the dislocation overlapping, made ECCI measurement irrelevant while some values could still be obtained from TEM measurements. We guess that this was due to the fact that for those high-density values, it could be possible with TEM to perform images close to the thin foil hole, i.e. in very thin areas, while the measurements depth is fixed for SEM-ECCI measurements to the accelerating voltage chosen. For ECCI measurements, the main uncertainty arises from the probed depth determination. The probed depth was assumed to be equal to $3\xi_g$ [49] but some author also provide values of $5\xi_g$ [62]. In the present case, the choice of $3\xi_g$ seem to better reproduce TEM observations.

XRD measurements indicate an almost similar dislocation density for austenite and ferrite deformed at 5 and 10%, which is not representative of the microstructure expected. Sidor *et al.* [63] also observed this saturation in XRD measurements in a cold rolled aluminum alloy. The densities obtained between two rolling steps remain equal to $(1.2 \pm 0.2) \times 10^{14}\ \mathrm{m}^{-2}$. This effect can be partly explained by the dynamic equilibrium between dislocation multiplication and annihilation, giving a saturation of the dislocation density. Moreover, in the case studied here, the formation of martensite has not been taken into account. 316L steels are mainly composed of austenite which, during deformation, transforms into martensite, thus decreasing the size of the crystallites, as shown by Han *et al.* [64] or Gubicza *et al.* [65]. The formation of this third phase in the steel studied here will therefore reduce the crystallite size D of the observed phases, which will increase the value of the density ρ_D (in equation (13)) for the 10% deformed sample.

However, XRD measurements are global measurements and should allow for the determination of SSDs densities, such as TEM and ECCI. Indeed, Lee *et al.* [66] reproduced a torsionally deformed copper sample with a Finite Element Method (FEM). They were able to compare their simulated value with the experimental TEM and XRD measurement. This allowed them to conclude that the dislocation density measured by XRD was located inside the cells, *i.e.* ρ_c. Even if the uncertainty in the measurement without deformation is very large for XRD measurements, the determined values are in the same range as the ones obtained by TEM/ECCI. The increase observed for 5% and 10% in the ferrite is in fairly well agreement with the results obtained with the imaging techniques. However, for austenite, there is a much larger discrepancy between XRD and the imaging techniques. However, one can see that the obtained measures are always slightly larger than the one obtained from ECCI/TEM. A first reason for that could be the invisibility criterion, where only part of the dislocations can be visible at the same time from ECCI/TEM measurements. Moreover, TEM and ECCI measurements are subjected to surface effects. Surface dislocation are always subjected to the image force, that tends to attract them to the surface. There is a relaxation of the dislocation structure near the free surfaces of the sample, which extends about approximately $65\ \mathrm{nm}$ into the sample as demonstrated by Field *et al.* [67]. In the case of TEM, measurements are performed on a thin film with a small thickness (about $146 \pm 10\ \mathrm{nm}$), therefore, the image force cannot be neglected, and the dislocation density is underestimated. Kohnert *et al.* [68] determined that the structure of a bcc steel loses 40% of the dislocations it contains, once in the state of a thin blade.

2) GND measurement (HR EBSD and EBSD)

The HR-EBSD method enables to visualize the expected localization of the deformation at grain boundaries for this microstructure, Figure 5. This phenomenon, which is explained by the incompatibility of the deformation between the two phases, is often observed in Duplex steels, [69] but also in Dual Phase steels [70].

Taking the average GND density on these maps seems to be biased since the disorientation is mainly located at the grain boundaries and there are very few grains present in totality on the maps. Moreover,

as the results obtained by the two methods seem to converge for large deformations, the significant data storage (about 15 GB per map) and post-processing required by the HR-EBSD technique is no longer justified, and standard EBSD can be preferred. Which is because the uncertainty of indexing on the disorientation axis becomes less critical as the angular disorientation is increasing. That is why HR-EBSD measurements should be preferred at small deformation, where the contribution of elastic strains are not negligible and for which the lower sensitivity of an indexing-based approach is preventing fine dislocation structures from being observed and quantified. In severely deformed materials, the degradation of the diffraction contrast in Kikuchi patterns strongly degrades the accuracy of HR-EBSD measurements. The slower acquisition speed and significant data storage associated with this technique is therefore no more justified. In between, a synergy of EBSD and HR-EBSD is expected. The first one provides statistics while the second one can be applied to further investigate local details of the microstructure.

Finally, one must be cautions in the interpretation of GND mappings, especially when derived from Euler angles (EBSD). As pointed out in **Figure 4** and **Figure 6**, GND mappings are sensible to orientation noise and may present alleged dislocation walls, whereas they are artifacts. The latter typically result from a discretization of orientations, which occurs when using dictionary indexing techniques [71] or applying spatial filters (Kuhawara…). Smoothing orientations to reduce noise in GND mappings is also not advisable, GND accounting for discontinuities in the crystal orientations. Regarding HR-EBSD analyses, possible artifacts rather stem from drift during acquisition. Because of the higher sensitivity of the method, drift may become visible in form of horizontal bands. The falsely associated GND density is however closer to the noise floor than what is seen in **Figure 4**(f) with EBSD.

3) Discussion about the relative amount of GND and SSD

Although dislocation imaging by TEM or ECCI allows us to see both GND and SSD dislocations, it allows mainly the measurement of ρ_c, *i.e.* mainly SSD. An average is performed from the XRD, TEM and ECCI measurements to obtain a value of ρ_{SSD} which is compared to the measurement obtained by HR-EBSD, ρ_{GND}. In Figure 10, the ρ_{GND} and ρ_{SSD} density is almost identical in the undeformed sample. During deformation, GND densities increase faster than SSD, especially for the 10% deformed sample. This is consistent with the fact that the early stages of deformation are driven by austenite, as described by Zhang *et al* [57]. However, the values obtained in this study seem to contradict what is expected in the literature. Zheng et al [72] found from a high-energy XRD and TEM experiment in a pearlitic ferritic steel that the density of GND is 10 times greater than that of SSD during deformation. In the 10% deformed sample, the density of GND is only twice that of SSD. Furthermore, the factor of 2 measured on the 10% sample seems to be inconsistent with what was found with mechanical models by Zhi et al. namely about twice as many SSD as GND during deformation in a TWIP steel [73].

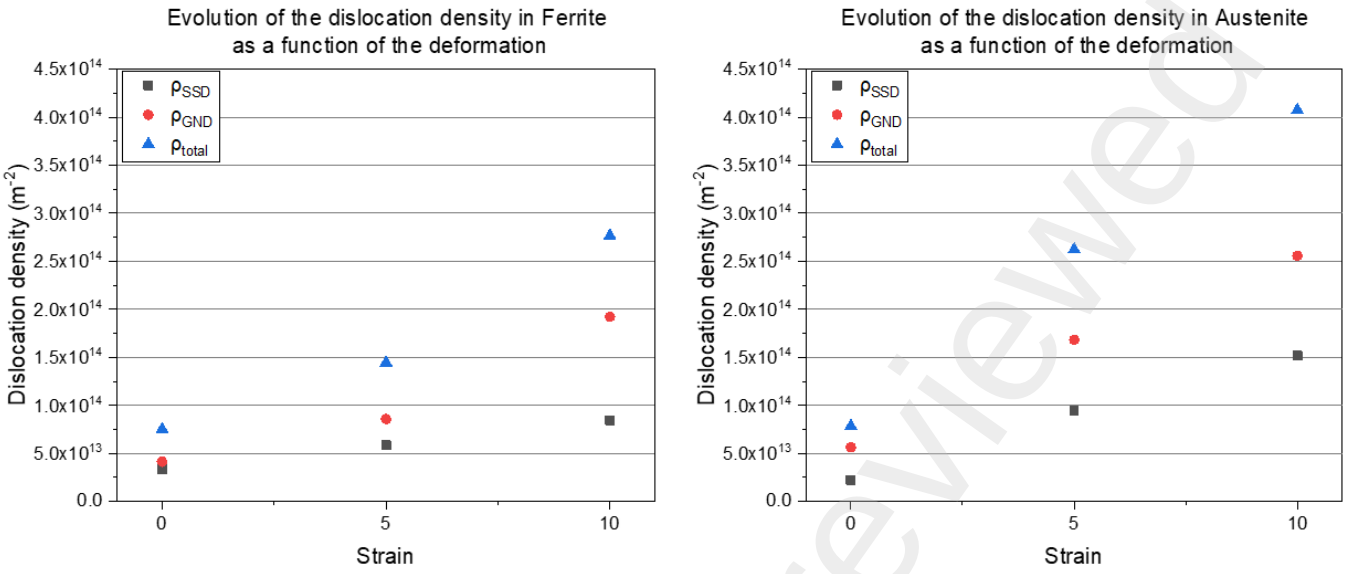

Figure 10: Comparison of measured dislocation densities as a function of strain. With ρ_{SSD}, the average of measurements obtained with XRD,TEM and SEM imaging, ρ_{GND} the measurement obtained with HR-EBSD and ρ_{total} the addition of ρ_{SSD} and ρ_{GND}. For (a) austenite and (b) ferrite, in the undeformed, 5% and 10% deformed samples.

4) Towards the prediction of yield stress

In the field of metallurgy, mechanical models are commonly used to predict the characteristics of a material. The dislocation density used in these models is often characterized by a single method. However, each method can only see a portion of the dislocations contained in the material. Even if the density most often used is the density initially present in the material, the acquisition parameters or the choice of the area can vary the result obtained and thus distort the model. For example, in a model describing the mechanical behavior of ferrite, the contribution to the yield stress σ_y is described by the term σ_R (which is the forest dislocation hardening or isotropic hardening) and is formulated by:

$$\sigma_R = \alpha_T M_T \mu b_{111} \sqrt{\rho_0}, \quad (14)$$

where α_T is the forest hardening coefficient, M_T is the Taylor factor, μ is the elastic shear modulus, b_{111} is the burger vector (other possible directions of the burger vector are neglected). The model and the values of the constants used were taken from the study by Mathevon *et al.* [70]. When using the different values of the dislocation density obtained by the different methods, the values of σ_R differ by 76 Mpa between $\rho_{Clustering}$ and ρ_{total} (see table 7).

Table 7: isotropic hardening obtained from the values of the different types of initial densities measured in the ferrite.

	ρ_0 (m^{-2})	σ_R(Mpa)
$\rho_{Clustering}$	$(2.5 \pm 0.1) \times 10^{13}$	104 ± 3
ρ_{TEM}	$(1.2 \pm 0.1) \times 10^{13}$	72 ± 3
ρ_{XRD}	$(6.1 \pm 13.1) \times 10^{13}$	162 ± 124
$\rho_{HR-EBSD}$	$(4.2 \pm 1.1) \times 10^{13}$	135 ± 19

ρ_{EBSD}	$(4.6 \pm 1.4) \times 10^{13}$	141 ± 23
$\rho_{SSD+GND}$	7.5×10^{13}	180

Mathevon *et al.* obtained an σ_R value of 109 Mpa in undeformed ferrite. It would be easy to say that R-ECCI+Clustering is the closest, but the model does not consider the austenitic phase and a large uncertainty remains on the volume explored in ECCI. Moreover, if we consider the loss of 40% of the dislocations contained in the thin foil [68], the measurements obtained by TEM imaging become equivalent to ECCI. This simple calculation shows that it of great importance to know what is observed using each characterization technique, for later use in micromechanical model.

5. Conclusion

In this study, several approaches for measuring dislocation density in deformed and undeformed materials were compared. XRD, EBSD, HR-EBSD, TEM and ECCI imaging were used to obtain the dislocation density present in industrial steel samples composed of austenite and ferrite phases for the following strain rates: 0, 5 and 10%.

Imaging methods saturate for densities above $10^{14}\ \mathrm{m}^2$. Density obtained by XRD is always high and not very accurate for low densities. The HR-EBSD and classical EBSD methods seem to be more versatile, for all observed densities and the increase de la densité de dislocation with the strain is well capture by EBSD or HR-HEBSD. At the grain scale, the GND density obtained with both method is very similar. Locally, dislocations structures and strain concentration are better evidenced using the HR-EBSD technique.

Imaging techniques such as TEM and ECCi, as well as XRD, primarily measure the contribution of SSDs.

EBSD and HR-EBSD mainly measure the GND denisty. In this case: EBSD and HR-EBSD measurements (GND) are always higher than TEM, ECCI and XRD measurements (SSD), and they are located at the grain boundaries.

The ratio between SSD and GND varies with the level of deformation, for the highest cases there are twice as many GND as SSD. These differences directly affect the calculation of hardening in micromechanical models, and must be carefully chosen.

Acknowledgements

This work was carried out as part of the DISCO (Dislocation Imaging in Scanning electron microsCOpy) project supported by the institut Carnot Ingénierie@Lyon. The authors acknowledge Nicholas Blanchard for access to the TEM JEOL 2010 of the Centre Lyonnais de Microscopy (www.clym.fr).

References

[1] J. Blaizot, T. Chaise, D. Nélias, M. Perez, S. Cazottes, P. Chaudet, Constitutive model for nickel alloy 690 (Inconel 690) at various strain rates and temperatures, Int. J. Plast. 80 (2016) 139–153.
[2] G. Krauss, Deformation and fracture in martensitic carbon steels tempered at low temperatures, Metall. Mater. Trans. B. 32 (2001) 205–221.
[3] M. Saeglitz, G. Krauss, Deformation, fracture, and mechanical properties of low-temperature-tempered martensite in SAE 43xx steels, Metall. Mater. Trans. A. 28 (1997) 377–387.
[4] C. Singh, A. Basu, G. Thomas, Quality of coal in integrated iron and steel plants in India with reference to available raw materials, J Inst EngIndia Min Met. DivIndia. 58 (1978).
[5] H. Mecking, U.F. Kocks, Kinetics of flow and strain-hardening, Acta Metall. 29 (1981) 1865–1875.
[6] U.F. Kocks, H. Mecking, Physics and phenomenology of strain hardening: the FCC case, Prog. Mater. Sci. 48 (2003) 171–273.
[7] Y. Estrin, H. Mecking, A unified phenomenological description of work hardening and creep based on one-parameter models, Acta Metall. 32 (1984) 57–70.
[8] Y. Estrin, Constitutive modelling of creep of metallic materials: Some simple recipes, Mater. Sci. Eng. A. 463 (2007) 171–176.
[9] J. Blaizot, Etude de l'influence des procédés de fabrication sur les propriétés mécaniques des alliages de nickel, Université de Lyon, 2016.
[10] P. Diano, A. Muggeo, J.C. Van Duysen, M. Guttmann, Relationship between microstructure and mechanical properties of Alloy 690 tubes for steam generators, J. Nucl. Mater. 168 (1989) 290–294.
[11] A. Borbély, J.H. Driver, T. Ungár, An X-ray method for the determination of stored energies in texture components of deformed metals; application to cold worked ultra high purity iron, Acta Mater. 48 (2000) 2005–2016. https://doi.org/10.1016/S1359-6454(99)00457-7.
[12] A. Wauthier-Monnin, T. Chauveau, O. Castelnau, H. Réglé, B. Bacroix, The evolution with strain of the stored energy in different texture components of cold-rolled IF steel revealed by high resolution X-ray diffraction, Mater. Charact. 104 (2015) 31–41. https://doi.org/10.1016/j.matchar.2015.04.005.
[13] J.F. Nye, Some geometrical relations in dislocated crystals, Acta Metall. 1 (1953) 153–162. https://doi.org/10.1016/0001-6160(53)90054-6.
[14] A.H. Cottrell, The mechanical properties of matter, (1964).
[15] M.F. Ashby, The deformation of plastically non-homogeneous materials, Philos. Mag. J. Theor. Exp. Appl. Phys. 21 (1970) 399–424.
[16] S. Birosca, G. Liu, R. Ding, J. Jiang, T. Simm, C. Deen, M. Whittaker, The dislocation behaviour and GND development in a nickel based superalloy during creep, Int. J. Plast. 118 (2019) 252–268.
[17] J. Zhang, B. Wang, H. Wang, Geometrically necessary dislocations distribution in face-centred cubic alloy with varied grain size, Mater. Charact. 162 (2020) 110205.
[18] D.A. Hughes, N. Hansen, D.J. Bammann, Geometrically necessary boundaries, incidental dislocation boundaries and geometrically necessary dislocations, Scr. Mater. 48 (2003) 147–153.
[19] D.G. Brandon, Y. Komem, Quantitative analysis of dislocation distributions, Metallography. 3 (1970) 111–126. https://doi.org/10.1016/0026-0800(70)90010-8.

[20] D.B. Williams, C.B. Carter, Transmission electron microscopy: a textbook for materials science, 2nd ed, Springer, New York, 2008.
[21] G. L'hôte, C. Lafond, P. Steyer, S. Deschanel, T. Douillard, C. Langlois, S. Cazottes, Rotational-Electron Channeling Contrast Imaging analysis of dislocation structure in fatigued copper single crystal, Scr. Mater. 162 (2019) 103–107. https://doi.org/10.1016/j.scriptamat.2018.10.050.
[22] S. Cazottes, A. Bechis, C. Lafond, G. L'Hôte, C. Roth, T. Dreyfus, P. Steyer, T. Douillard, C. Langlois, Toward an automated tool for dislocation density characterization in a scanning electron microscope, Mater. Charact. 158 (2019) 109954. https://doi.org/10.1016/j.matchar.2019.109954.
[23] W. Pantleon, Resolving the geometrically necessary dislocation content by conventional electron backscattering diffraction, Scr. Mater. 58 (2008) 994–997. https://doi.org/10.1016/j.scriptamat.2008.01.050.
[24] B.S. El-Dasher, B.L. Adams, A.D. Rollett, Viewpoint: experimental recovery of geometrically necessary dislocation density in polycrystals, Scr. Mater. 48 (2003) 141–145. https://doi.org/10.1016/S1359-6462(02)00340-8.
[25] S. Sun, B.L. Adams, W.E. King, Observations of lattice curvature near the interface of a deformed aluminium bicrystal, Philos. Mag. A. 80 (2000) 9–25. https://doi.org/10.1080/01418610008212038.
[26] D.J. Prior, Problems in determining the misorientation axes, for small angular misorientations, using electron backscatter diffraction in the SEM., J. Microsc. 195 (1999) 217–225.
[27] J. Wheeler, E. Mariani, S. Piazolo, D.J. Prior, P. Trimby, M.R. Drury, The Weighted Burgers Vector: a new quantity for constraining dislocation densities and types using electron backscatter diffraction on 2D sections through crystalline materials., J. Microsc. 233 (2009) 482–494. https://doi.org/10.1111/j.1365-2818.2009.03136.x.
[28] A.J. Wilkinson, D. Randman, Determination of elastic strain fields and geometrically necessary dislocation distributions near nanoindents using electron back scatter diffraction, Philos. Mag. 90 (2010) 1159–1177. https://doi.org/10.1080/14786430903304145.
[29] C. Ernould, B. Beausir, J.-J. Fundenberger, V. Taupin, E. Bouzy, Chapter Five - Applications of the method, in: M. Hÿtch, P.W. Hawkes (Eds.), Adv. Imaging Electron Phys., Elsevier, 2022: pp. 155–215. https://doi.org/10.1016/bs.aiep.2022.07.005.
[30] A.J. Wilkinson, G. Meaden, D.J. Dingley, High-resolution elastic strain measurement from electron backscatter diffraction patterns: New levels of sensitivity, Ultramicroscopy. 106 (2006) 307–313. https://doi.org/10.1016/j.ultramic.2005.10.001.
[31] T. Vermeij, J.P.M. Hoefnagels, A consistent full-field integrated DIC framework for HR-EBSD, Ultramicroscopy. 191 (2018) 44–50. https://doi.org/10.1016/j.ultramic.2018.05.001.
[32] T.J. Ruggles, G.F. Bomarito, R.L. Qiu, J.D. Hochhalter, New levels of high angular resolution EBSD performance via inverse compositional Gauss–Newton based digital image correlation, Ultramicroscopy. 195 (2018) 85–92. https://doi.org/10.1016/j.ultramic.2018.08.020.
[33] Q. Shi, S. Roux, F. Latourte, F. Hild, Estimation of elastic strain by integrated image correlation on electron diffraction patterns, Ultramicroscopy. 199 (2019) 16–33. https://doi.org/10.1016/j.ultramic.2019.02.001.
[34] C. Ernould, B. Beausir, J.-J. Fundenberger, V. Taupin, E. Bouzy, Global DIC approach guided by a cross-correlation based initial guess for HR-EBSD and on-axis HR-TKD, Acta Mater. 191 (2020) 131–148. https://doi.org/10.1016/j.actamat.2020.03.026.
[35] C. Ernould, B. Beausir, J.-J. Fundenberger, V. Taupin, E. Bouzy, Advances in Imaging and Electron Physics, Volume 223, Edited by Martin Hÿtch, Peter W. Hawkes, Elsevier, 2022.
[36] E. Kröner, Kontinuumstheorie der Versetzungen und Eigenspannungen, Springer-Verlag, Berlin Heidelberg, 1958. https://www.springer.com/de/book/9783540022619.
[37] S. Kalácska, Z. Dankházi, G. Zilahi, X. Maeder, J. Michler, P.D. Ispánovity, I. Groma, Investigation of geometrically necessary dislocation structures in compressed Cu micropillars by 3-dimensional HR-EBSD, Mater. Sci. Eng. A. 770 (2020) 138499. https://doi.org/10.1016/j.msea.2019.138499.

[38] S.S. Dhinwal, C. Ernould, B. Beausir, Facilitating the occurrence of dynamic recrystallization in plain extra low-carbon steel by warm asymmetric rolling, Mater. Charact. 189 (2022) 111942. https://doi.org/10.1016/j.matchar.2022.111942.
[39] C. Ernould, B. Beausir, J.-J. Fundenberger, V. Taupin, E. Bouzy, Characterization at high spatial and angular resolutions of deformed nanostructures by on-axis HR-TKD, Scr. Mater. 185 (2020) 30–35. https://doi.org/10.1016/j.scriptamat.2020.04.005.
[40] J. Jiang, T.B. Britton, A.J. Wilkinson, Evolution of dislocation density distributions in copper during tensile deformation, Acta Mater. 61 (2013) 7227–7239. https://doi.org/10.1016/j.actamat.2013.08.027.
[41] T. Ungar, H. Mughrabi, D. Rönnpagel, M. Wilkens, X-ray line-broadening study of the dislocation cell structure in deformed [001]-orientated copper single crystals, Acta Metall. 32 (1984) 333–342. https://doi.org/10.1016/0001-6160(84)90106-8.
[42] D.G. Brandon, Y. Komem, Quantitative analysis of dislocation distributions, Metallography. 3 (1970) 111–126.
[43] D.B. Williams, C.B. Carter, Transmission electron microscopy: a textbook for materials science, 2nd ed, Springer, New York, 2008.
[44] D.J.H. Cockayne, I.L.F. Ray, M.J. Whelan, Investigations of dislocation strain fields using weak beams, Philos. Mag. 20 (1969) 1265–1270.
[45] P.B. Hirsch, F.J. Humphreys, The deformation of single crystals of copper and copper-zinc alloys containing alumina particles-I. Macroscopic properties and workhardening theory, Proc. R. Soc. Lond. Math. Phys. Sci. 318 (1970) 45–72.
[46] S. Cazottes, A. Bechis, C. Lafond, G. L'Hôte, C. Roth, T. Dreyfus, P. Steyer, T. Douillard, C. Langlois, Toward an automated tool for dislocation density characterization in a scanning electron microscope, Mater. Charact. 158 (2019) 109954. https://doi.org/10.1016/j.matchar.2019.109954.
[47] J. Gallet, M. Perez, S. Dubail, T. Chaise, T. Douillard, C. Langlois, S. Cazottes, About the automatic measurement of the dislocation density obtained by R-ECCI, Mater. Charact. (2022) 112358. https://doi.org/10.1016/j.matchar.2022.112358.
[48] C. Lafond, T. Douillard, S. Cazottes, P. Steyer, C. Langlois, Electron CHanneling ORientation Determination (eCHORD): An original approach to crystalline orientation mapping, Ultramicroscopy. 186 (2017). https://doi.org/10.1016/j.ultramic.2017.12.019.
[49] S. Zaefferer, N.-N. Elhami, Theory and application of electron channelling contrast imaging under controlled diffraction conditions, Acta Mater. 75 (2014) 20–50. https://doi.org/10.1016/j.actamat.2014.04.018.
[50] B. Beausir, J.-J. Fundenberger, Analysis Tools for Electron and X-ray diffraction, ATEX - software, (2017). www.atex-software.eu.
[51] C. Ernould, B. Beausir, J.-J. Fundenberger, V. Taupin, E. Bouzy, Integrated correction of optical distortions for global HR-EBSD techniques, Ultramicroscopy. 221 (2021) 113158. https://doi.org/10.1016/j.ultramic.2020.113158.
[52] J. Jiang, T.B. Britton, A.J. Wilkinson, Measurement of geometrically necessary dislocation density with high resolution electron backscatter diffraction: effects of detector binning and step size, Ultramicroscopy. 125 (2013) 1–9.
[53] C. Fressengeas, B. Beausir, C. Kerisit, A.-L. Helbert, T. Baudin, F. Brisset, M.-H. Mathon, R. Besnard, N. Bozzolo, On the evaluation of dislocation densities in pure tantalum from EBSD orientation data, Matér. Tech. 106 (2018) 604. https://doi.org/10.1051/mattech/2018058.
[54] L. Lutterotti, Maud: a Rietveld analysis program designed for the internet and experiment integration, Acta Crystallogr A. 56 (2000) s54.
[55] S. Murugesan, P. Kuppusami, E. Mohandas, M. Vijayalakshmi, X-Ray Diffraction Analysis of Defects in Cold Worked Type 316 Stainless Steel, in: AIP Conf. Proc., American Institute of Physics, 2011: pp. 485–486.
[56] S. Murugesan, P. Kuppusami, E. Mohandas, M. Vijayalakshmi, X-ray diffraction Rietveld analysis of cold worked austenitic stainless steel, Mater. Lett. 67 (2012) 173–176.

[57] X. Zhang, P. Wang, D. Li, Y. Li, Multi-scale study on the heterogeneous deformation behavior in duplex stainless steel, J. Mater. Sci. Technol. 72 (2021) 180–188. https://doi.org/10.1016/j.jmst.2020.09.023.
[58] T. Ungár, J. Gubicza, G. Ribárik, A. Borbély, Crystallite size distribution and dislocation structure determined by diffraction profile analysis: principles and practical application to cubic and hexagonal crystals, J. Appl. Crystallogr. 34 (2001) 298–310.
[59] D. Louër, J.P. Auffrédic, J.I. Langford, D. Ciosmak, J.C. Niepce, A precise determination of the shape, size and distribution of size of crystallites in zinc oxide by X-ray line-broadening analysis, J. Appl. Crystallogr. 16 (1983) 183–191.
[60] G. Caglioti, A. t Paoletti, F.P. Ricci, Choice of collimators for a crystal spectrometer for neutron diffraction, Nucl. Instrum. 3 (1958) 223–228.
[61] S.Y.P. Allain, O. Bouaziz, I. Pushkareva, C.P. Scott, Towards the microstructure design of DP steels: A generic size-sensitive mean-field mechanical model, Mater. Sci. Eng. A. 637 (2015) 222–234.
[62] A.J. Wilkinson, G.R. Anstis, J.T. Czernuszka, N.J. Long, P.B. Hirsch, Electron channelling contrast imaging of interfacial defects in strained silicon-germanium layers on silicon, Philos. Mag. A. 68 (1993) 59–80. https://doi.org/10.1080/01418619308219357.
[63] J.J. Sidor, P. Chakravarty, J.G. Bátorfi, P. Nagy, Q. Xie, J. Gubicza, Assessment of Dislocation Density by Various Techniques in Cold Rolled 1050 Aluminum Alloy, Metals. 11 (2021) 1571.
[64] J.-K. Han, X. Liu, I. Lee, Y.O. Kuzminova, S.A. Evlashin, K.-D. Liss, M. Kawasaki, Structural evolution during nanostructuring of additive manufactured 316L stainless steel by high-pressure torsion, Mater. Lett. 302 (2021) 130364.
[65] J. Gubicza, M. El-Tahawy, Y. Huang, H. Choi, H. Choe, J.L. Lábár, T.G. Langdon, Microstructure, phase composition and hardness evolution in 316L stainless steel processed by high-pressure torsion, Mater. Sci. Eng. A. 657 (2016) 215–223.
[66] D.J. Lee, E.Y. Yoon, D.-H. Ahn, B.H. Park, H.W. Park, L.J. Park, Y. Estrin, H.S. Kim, Dislocation density-based finite element analysis of large strain deformation behavior of copper under high-pressure torsion, Acta Mater. 76 (2014) 281–293.
[67] D.P. Field, K.R. Magid, I.N. Mastorakos, J.N. Florando, D.H. Lassila, J.W. Morris Jr, Mesoscale strain measurement in deformed crystals: A comparison of X-ray microdiffraction with electron backscatter diffraction, Philos. Mag. 90 (2010) 1451–1464.
[68] A.A. Kohnert, H. Tummala, R.A. Lebensohn, C.N. Tomé, L. Capolungo, On the use of transmission electron microscopy to quantify dislocation densities in bulk metals, Scr. Mater. 178 (2020) 161–165.
[69] H. Khatami-Hamedani, A. Zarei-Hanzaki, H.R. Abedi, A.S. Anoushe, L.P. Karjalainen, Dynamic restoration of the ferrite and austenite phases during hot compressive deformation of a lean duplex stainless steel, Mater. Sci. Eng. A. 788 (2020) 139400.
[70] A. Mathevon, Caractérisation et modélisation des évolutions microstructurales et des propriétés mécaniques durant le traitement thermique d'aciers Dual-Phase, (2020).
[71] Y.-H. Chen, S.U. Park, D. Wei, G. Newstadt, M. Jackson, J.P. Simmons, M. De Graef, A.O. Hero, A Dictionary Approach to EBSD Indexing, ArXiv150207436 Phys. Stat. (2015). http://arxiv.org/abs/1502.07436 (accessed March 5, 2019).
[72] C. Zheng, L. Li, Y. Wang, W. Yang, Z. Sun, Micromechanical behavior of eutectoid steel quantified by an analytical model calibrated by in situ synchrotron-based X-ray diffraction, Mater. Sci. Eng. A. 631 (2015) 181–188. https://doi.org/10.1016/j.msea.2015.02.003.
[73] H. Zhi, C. Zhang, S. Antonov, H. Yu, T. Guo, Y. Su, Investigations of dislocation-type evolution and strain hardening during mechanical twinning in Fe-22Mn-0.6C twinning-induced plasticity steel, Acta Mater. 195 (2020) 371–382. https://doi.org/10.1016/j.actamat.2020.05.062.